Comparison of the Measured and Analytical Response Profiles of a 3.3 to 15.5 μ Imaging System and the Effect of Detector Diffusion

C. F. Bruce Jr.
Jet Propulsion Laboratory, Pasadena, CA 91109
California Institute of Technology

ABSTRACT

This paper provides an overview of the Tropospheric Emission Spectrometer (TES) and its mission, as a part of NASA's Earth Observing System (EOS). The design of the re-imaging system and its detectors and the test set-up used to characterize the field of view response will be presented. Measured system optical response profiles will be presented for each of the four infrared spectral bands (3.5-5.3, 5.1-9.1, 8.3-12.2 and 11.1 – 15.4 μ) supported by TES. Specific emphasis will be placed upon the comparison of these measured optical response functions with the results of an analytic model of the response. The model includes a simple yet accurate representation of the detector response function, which includes the photo-generated electron's diffusion length.

Keywords: Detector, HgCdTe, Lateral Diffusion Length, Spatial Response.

1. INTRODUCTION

1.1 THE TES MISSION and INSTRUMENT ARCHITECTURE

The Tropospheric Emission Spectrometer instrument is one of four instruments scheduled to fly aboard the Earth Observing System (EOS), AURA satellite. AURA is currently scheduled for launch in January of '04. The goals of the EOS program have been summarized in five "research questions" as reviewed in the TES Science Requirements[1].

1) What are the nature and extent of land–cover and land-use change and the consequences for sustained productivity?

2) How can we enable regionally useful forecasts of precipitation and temperature on seasonal to inter-annual time frames?

3) Can we learn to predict natural hazards and mitigate natural disasters?

4) What are the causes and impacts of long-term climate variability and can we distinguish natural from human induced-drivers?

5) How and why are concentrations and distributions of atmospheric ozone changing?

Although TES may contribute to answering all five questions, TES is specifically designed to address item five and it will do this by providing global maps of chemical concentration through out the troposphere every five days. In order to accomplish this feat, TES has been designed as a high resolution Fourier Transform Spectrometer (FTS) which is capable of collecting infrared spectra over a large region of the infrared spectrum from 3.3 to 15.5 microns at high spectral resolution (.025 cm^-1).

The primary objective is to measure the global three-dimensional distribution of concentration of a large number of molecules important to tropospheric physics and chemistry. These important molecular species include: ozone, nitric oxide, nitrogen dioxide, nitric acid, water vapor, carbon monoxide, methane and carbon dioxide which is used for the determination of atmospheric temperature. TES will accomplish this through a series of nadir and limb measurements using 16-pixel, linear detector arrays in each of four infrared optical bands. In the limb view the 16 pixels' IFOVs will rise from the earth's surface to ~30 km at the top of the troposphere. Each pixel's IFOV will have a spatial extent of 2.3km high by 23 km parallel to the earth's surface at the limb. In the nadir view the pixel IFOV is 0.5 km along track by 5.0 km cross track.

1.2 THE TES OPTICAL CONFIGURATION

The TES optical system is divided into four major sub-elements; the gimbal optics, the fore optics telescope, the interferometer, and the Focal Plane Opto-Mechanical Assemblies (FPOMA). A drawing of the TES optical system is provided in figure 1.

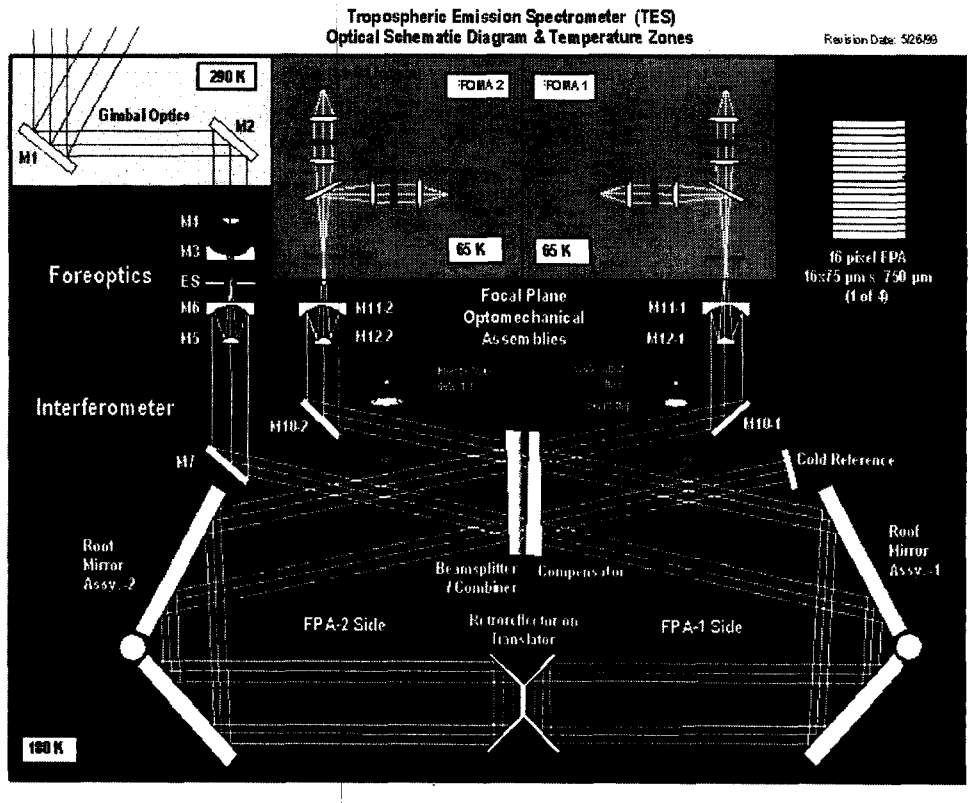

Figure 1: TES Optical Layout and Temperature Zones

There are two FPOMAs, which collect the output signal from the interferometer, band limit the light and re-image the signal onto an array of detectors. A cross sectional view of the FPOMA with its temperature zones identified is

provide in figure 2 along with a mechanical schematic of the exterior of the FPOMA. The output from the interferometer enters the FPOMA through an all aluminum F/8 Cassegrain telescope operating at 177K. The light

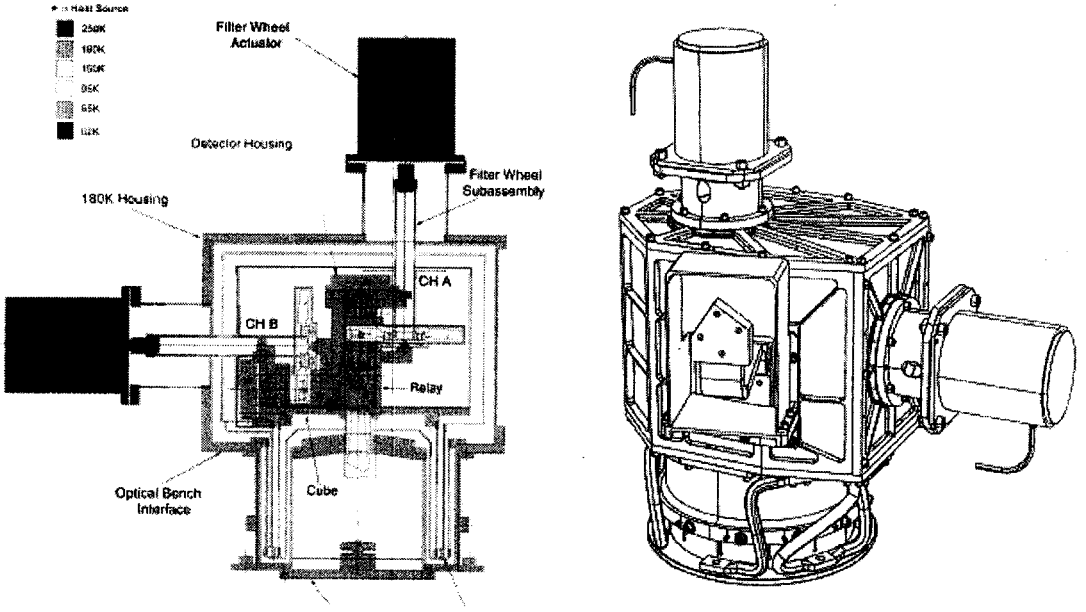

Figure 2: FPOMA Cross Section and Exterior View

from the telescope is re-imaged at a 65K field stop after which a dichroic beam splitter divides the light. The beam then enters one of two F/2 relays, which re-collimates the light before sending it through any of a number of filters in the cold filter wheel assembly. The light is then re-imaged onto the detector array at F/2. The FPOMA pupil is re-imaged at zero path difference in the interferometer. Optical ghost were designed to be < 0.1% within the field by tilting filters (3.5 deg.) and adjusting the field lenses' curvatures. The filters and dichroics are also wedged to prevent optical channeling. The 1A & 2 A band relay elements are ZnSe, the 1B relay elements are Germanium and the 2B relay elements are CdTe.

1.3 THE DETECTOR ARRAYS

The TES detector arrays are housed inside the FPOMAs at the focus of each relay. The detector arrays are implemented with a detector amplifier topology that includes one, differential J-FET buffered, transimpedance amplifier (TIA) per detector element.

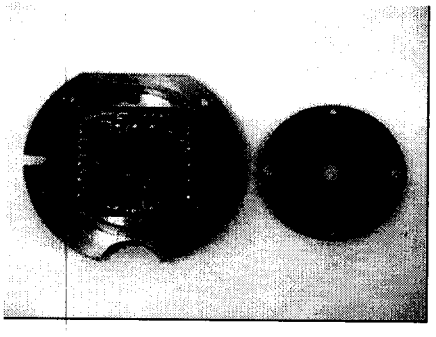

Picture 1: The 1A Detector and Package

The J-FETS, the feedback resistor and decoupling capacitors are placed with the linear detector arrays onto a ceramic, multilayer board (CMLB). A Be flange is mated to the CMLB using an adhesive. The Be flange provides the mechanical and thermal interfaces for the detector package. This detector package is shown in picture 1. Some detector parameters for each of the four spectral bands are summarized in table 1.

Parameter	Detector - 1A1	Detector - 2A1	Detector - 1B1	Detector - 2B1
x	0.283	0.2274	0.2207	0.204
Temperature (K)	65	65	65	65
Detector Optical Area (μm^2)	75 x 750	75 x 750	75 x 750	75 x 750
Detector Band Pass (μm)	3.3 - 5.3	5.1 - 9.1	8.3 - 12.2	11.1 - 15.5
Diffusion length (μm) (est.)	15	20	20-25	25-30

Table 1: TES Detector Parameters

The TES detector arrays are based on a HgCdTe, double-layer planar heterostructure (DLPH), lateral collection architecture[2, 3, 4, 5]

2. CRYOGENIC TEST SYSTEM

Once the detectors were integrated into the FPOMAs it was necessary to focus the detectors and align them to each of the boresight vectors of the FPOMAs and to each other within each FPOMA. Data on the detector location and FPOMA bore sights were collected by a cryogenic test set, which simulated the FPOMA interfaces with the TES instrument, both thermally and mechanically. The test set also provides a target stimulus and controller.

The stimulus consisted of an ambient; three axes scan mechanism, which positioned the slit, a blackbody to illuminate the slit, a collimator to relay the slit to the FPOMA, and a data acquisition system. The test chamber is a 4' vacuum chamber with a ZnSe window near the focus of the collimator. In side the vacuum chamber is the warm collimator with an effective focal length of 1.0 m, a 180K fold mirror, and a 180K reference reflector polished into the Invar mounting interface of the FPOMA.

The FPOMA and detectors require three thermal interfaces. The instrument-mounting interface at the entrance of the telescope is an invar interface at 177K. This interface was simulated with an invar plate cooled to 177 K while minimizing the distortion of the Invar plate. This was critical since the under side of this Invar plate is parallel to the top surface and polished to an optical quality finish. This polished annular reference surface was used to established the boresight vector of the FPOMAs and provide a reference for the location of the center of each of the 16 pixel arrays.

A 230K Al thermal shield cooled by a GN2 transfer system surrounds the entire FPOMA. The detectors are cooled to their 65K operating temperature through a copper strap, which was isolated by G10 stand offs and driven by a helium transfer system. The temperature was monitored at the end of the copper strap, which interfaced to the Al cold link of the FPOMA. The temperature control was stable to < +/- 1 K through most of the testing.

The optical background to the FPOMA was limited to levels similar to those expected from the instrument configuration. This was accomplished through the use of a 180K-fold mirror and an F/10 tube sunk to the 180K, cooling loop. The data was acquired through a multiple channel digital voltmeter, which scanned through the 32 detectors outputs. A PC with custom software managed the acquisition of data and stepped the positioning stage, which held the slit. The software provided control through automated macros and provided a real time plotting capability.

3. TEST RESULTS

A single scan axis data set, collected after the focus adjustments of each FPOMA were completed, is presented. A blackbody at 325 K illuminated the slit. In FPOMA 1, figure 4, the 1A1 and 1B1 filters were selected covering the pass bands of 4.44 - 5.26 microns and 9.52 - 12.20 microns respectively. Scans are acquired from left to right.

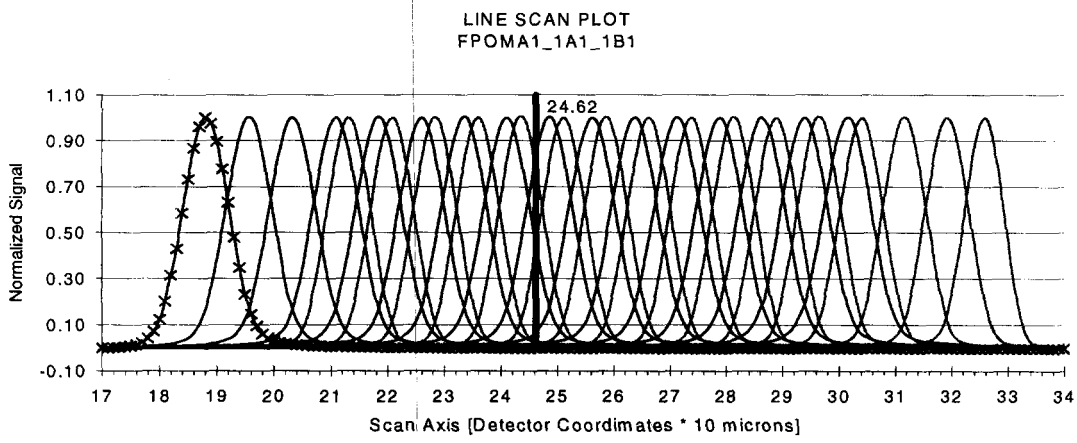

Figure 4: FPOMA1, Spatial Response Functions

The data for these scans was acquired at each 10-micron step of the slit. These sample points are explicitly shown for the first response function in each plot. Each scan required approximately 20 min to acquire. One high resolution scan taken with 1.0 micron steps of the slit was acquired to verify that there was no high frequency spatial information in the pixel response functions. This data (not shown) supports the use of the interpolated lines as an accurate representation of the data. The remainder of the data will be plotted as continuous functions for visual simplicity. The data for FPOMA1 shows a 225-micron misalignment in this axis, which was later corrected. The

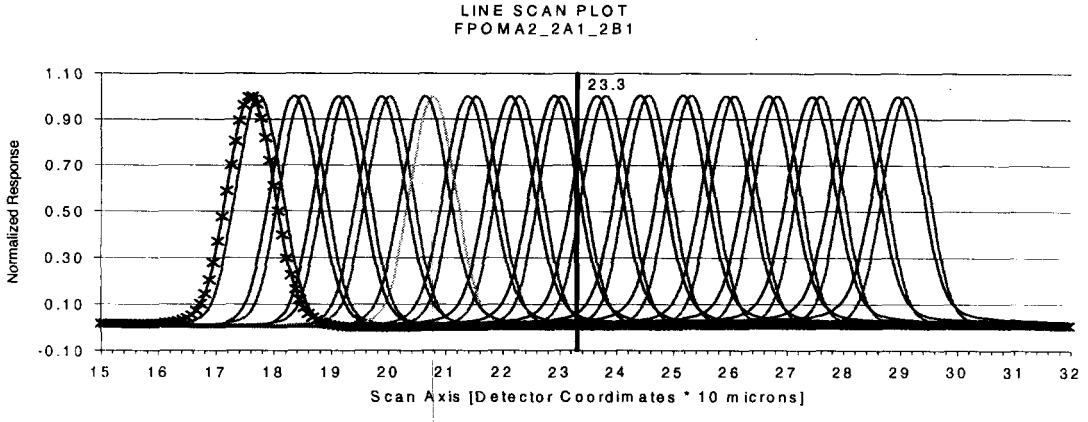

Figure 5: FPOMA2, Spatial Response Functions

response functions for each pixel with in a particular optical band pass are very uniform in shape. All of the data is corrected for gain and offset on a per pixel basis. The data for FPOMA 2, Figure 5, reveals a residual misalignment of 2 and 6 microns for the 2B1 and 2A1 channel respectively. In this case the 2A1and 2B1filter were used. These filters define an optical pass band of 7.55 – 9.10 microns and 11.11 – 15.38 microns respectively. Again the uniformity of detector response functions is excellent across the arrays after a two-point, gain and offset correction.

4. ANALYTICAL MODEL

An analysis was undertaken to compare the shape of the measured response functions with the theoretically predicted response functions. The method chosen for the analysis is to convolve the measured slit function with the theoretical optical response function of the FPOMA and the detector response function. An illustration of these functions is provided in figure 6. The measured data and analytic functions are then compared in section 5.0.

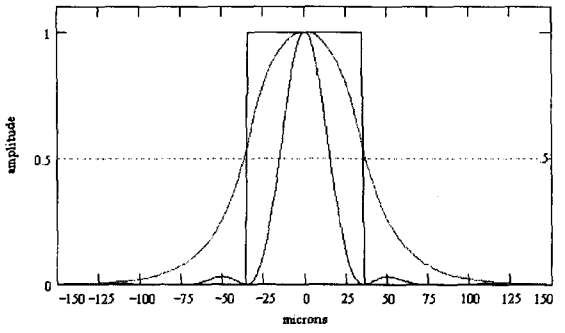

Figure 6: Convolved Functions

The slit function is defined as a normalized boxcar function of width equal to the slit width. The slit width was measured to be 70 microns. This function is the same for all convolutions. The detector response function is also normalized and is calculated by equation 1.0. This function is an excellent representation of a thin detector with a detector junction length less than the photo-generated electron's diffusion length. The function can be viewed as the probability density for the collection of a photoelectron by a detector junction of length J_d. The probability of any one collection is ~exp $(-x/L_d)$ integrated over the junction length (J_d). L_d is the diffusion length of the photo-generated electron and x is the vector from the electron's position to the detector junction.

$$D(x,X,L_d) := \left[\int_{\frac{-J_d}{2}}^{\frac{J_d}{2}} \exp\left[-\frac{|(x-X)-s|}{L_d} \right] ds \right] \tag{1.0}$$

The optical response function for the FPOMA is calculated as diffraction limited with a centrally obscured, circular aperture at F/2 (equation 2.0)[8]. This response function is then integrated over the specific optical pass band and weighted by the black body function and normalized to unity (equation 3.0).

$$S(x,y,X,\lambda) := \left| \left[\frac{1}{\left(1-\varepsilon^2\right)^2} \right] \left[\frac{2 \cdot J1\left[\frac{\pi \cdot \sqrt{(x-X)^2+y^2}}{\lambda \cdot F} \right]}{\frac{\pi \cdot \sqrt{(x-X)^2+y^2}}{\lambda \cdot F}} - \varepsilon^2 \cdot \left[\frac{2 \cdot J1\left[\left[\frac{\pi \cdot \sqrt{(x-X)^2+y^2}}{\lambda \cdot F} \right] \cdot \varepsilon \right]}{\left[\frac{\pi \cdot \sqrt{(x-X)^2+y^2}}{\lambda \cdot F} \right] \cdot \varepsilon} \right] \right]^2 \right| \tag{2.0}$$

$$SS(x,y,X,\lambda_1,\lambda_2) := \frac{\int_{\lambda_1}^{\lambda_2} B(\lambda,T) \cdot S(x,y,X,\lambda)\, d\lambda}{\int_{\lambda_1}^{\lambda_2} B(\lambda,T) \cdot 1\, d\lambda} \tag{3.0}$$

5. COMPARISON of RESULTS

The functions defined in section 4.0 were convolved for each of the four optical bands. Figure 7 shows a direct comparison between the analytic and measured response functions for each band. A diffusion length of 17 microns

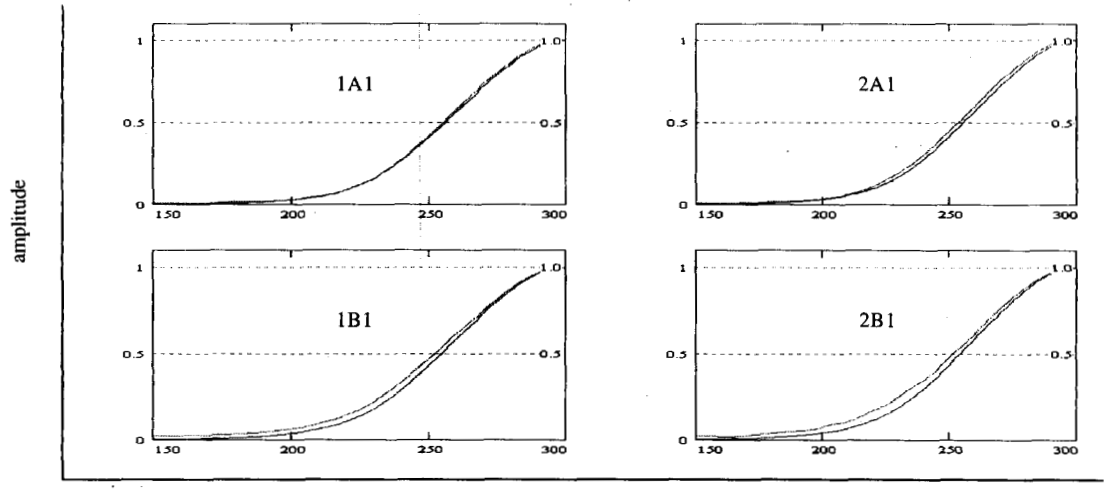

Figure 7: Comparison of measure and analytic response functions (Ld=17 microns)

was assumed for all the bands. Only the left half of the optical response function is shown in order to improve the visible detail in the plots. The band 1A results are nearly identical to the theoretical predictions for a diffraction limited system and a 17-micron photo-generated electron diffusion length. In each of the other cases the measured response function is slightly broader than the analytic function by an amount, which increases with wavelength from 1A to 2A to 1B and finally to 2B. The 2B exhibits the largest variance with the analytic result. Since the polychromatic optical response function has already accounted for the wavelength dependence of the analytic optical response function and the slit function has no wavelength dependence we postulate that the detector response function may be responsible for the observed discrepancy.

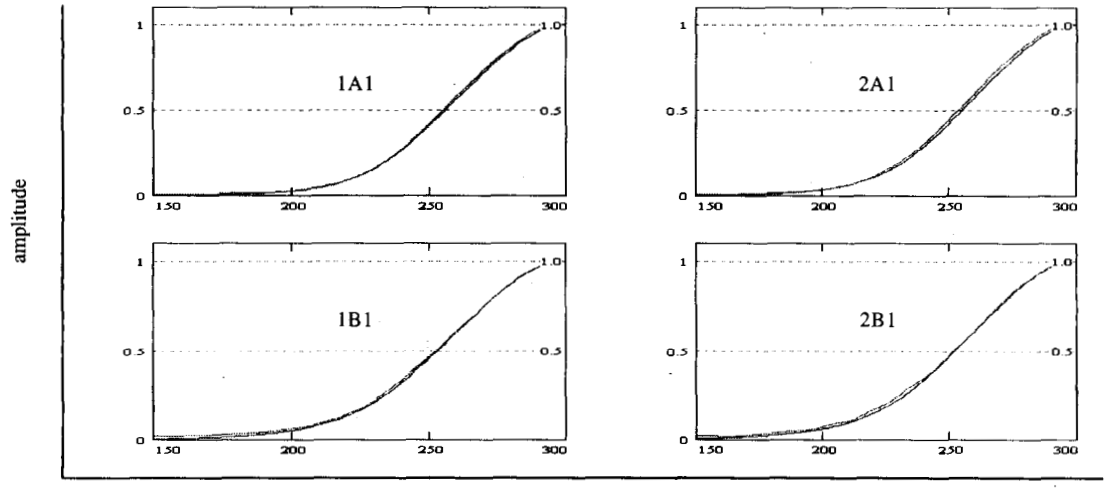

Figure 8: Comparison of measure and "best fit" analytic response functions (Ld=17,18,20,21 microns)

The detector diffusion length parameter is then selected to provide the best fit to the measured response data for each band. The diffusion length, which provides the best fits for the 1A, 2A, 1B and 2B, bands respectively are 17, 18, 20 and 21 microns. The results are shown in figure 8.

6. IMPLICATION for DETECTOR DIFFUSION

As shown in table 2, the actual predicted minority carrier diffusion length for each of the detectors is considerably larger than the diffusion lengths selected to fit the spatial response data shown in figure 8.

Detector	Detector L_{d} (μm)	Fitting L_{d} (μm)
1A	15	17
2A	20	18
1B	20-25	20
2B	25-30	21

Table 2: Detector Parameters

Clearly, the actual variability in the detector diffusion length, as shown in figure 9, would have a significant impact on the system response functions. However, the data, in figures 7 and 8, shows that it does not. In fact, the measured and predicted response functions are very similar without any lateral diffusion length fitting. If the

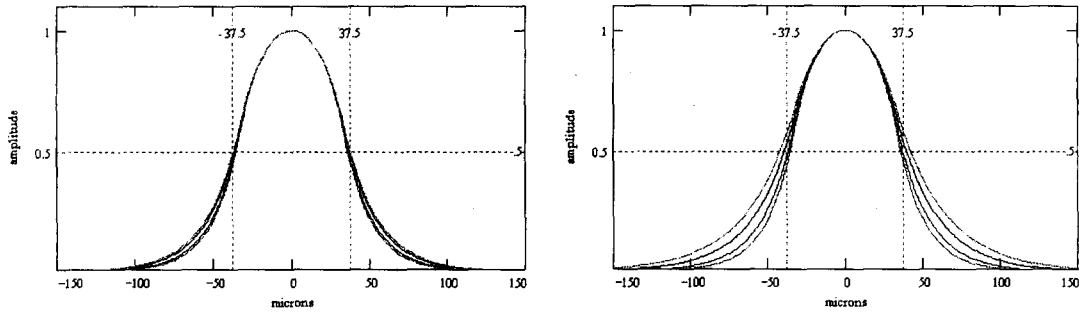

Figure 9: Detector Response Functions (Left: L_d=17,18,20,21μ) (Right: L_d = 17,20,25,30μ)

detector response model was a two-dimensional model, the absorber depth, which also increases with wavelength, might be the actual factor accounting for the slight broadening of the detector response function with increasing wavelength. In addition the detector minority carrier diffusion length may not be the same value as the photo-generated electron diffusion length[9] particularly away from the junction and so the use of the minority carrier diffusion length may result in an over estimate of the detector response function width[10]. As well, for the TES detector architecture the effect of neighboring pixels tends to reduce the spatial extent of an individual detector's response function much in the same way a guard band may be used to reduce the spatial extend of a pixel. For example, if an electron appears half way between two detector junctions only one junction will collect that electron and thus neighboring pixels through a competition for the signal, limit one another's spatial response function.

7. CONCLUSION

The field of view response of two cryogenic imaging systems covering four optical band passes were characterized. Each band pass has an HgCdTe detector array with a different cutoff wavelength. The complete field of view response was characterized and compared to an analytic model of the response function. It was determined that the variation of the detector diffusion length between optical bands did not significantly broaden the field of view response of this nearly diffraction limited system.

ACKNOWLEDGEMENT

The work described in this article was performed both at the Jet Propulsion Laboratory, California Institute of Technology and at its subcontractors under contract with the National Aeronautics and Space Administration.

The Space Dynamic Laboratory provided the FPOMAs to JPL under contract[6].

The Rockwell Science Center of Rockwell International provided the detector assemblies to JPL under contract[7].

Reference herein to any specific commercial product, process, or service by trade name, trade mark, manufacturer, or otherwise, does not constitute or imply its endorsement by the United States Government or the Jet Propulsion Laboratory, California Institute of Technology.

This work was funded by JPL Contract No. DAAB07-93-C-U505

REFERENCES

1. Reinhard Beer, TES, Scientific Objectives & Approach, Goals & Requirements Rev. 6, (1999).
2. J. Bajaj, etal, IRIS Specialty Group Infrared Detectors, ERIM, (1999).
3. W.V. McLevige, etal, IRIS Specialty Group Infrared Detectors, ERIM, (1999).
4. C.F. Bruce, etal, Infrared Detector Assemblies for the Tropospheric Emission Spectrometer, IEEE Aerospace Conference, IEEE, (2000).
5. Holloway (H. Holloway, *J. Appl. Phys.*, **49**, 4264, (1978).
6. Jet Propulsion Laboratory, National Aeronautics and Space Administration, Contract 961238, (2000).
7. Jet Propulsion Laboratory, National Aeronautics and Space Administration, Contract 961089, (2001).
8. D.J. Schroeder, *Astronomical Optics*, Ch. 10, Academic press, Inc., San Diego, 1987.
9. M.B. Reine, *Photovoltaic Detectors in HgCdTe*, prepublication notes, Feb. 27th, 2000.
10. V. Gopal, Resistance area product of diodes in a long-wavelength infrared HgCdTe mosaic array, Infrared Physics and Technology, Vol. 43, (2000).

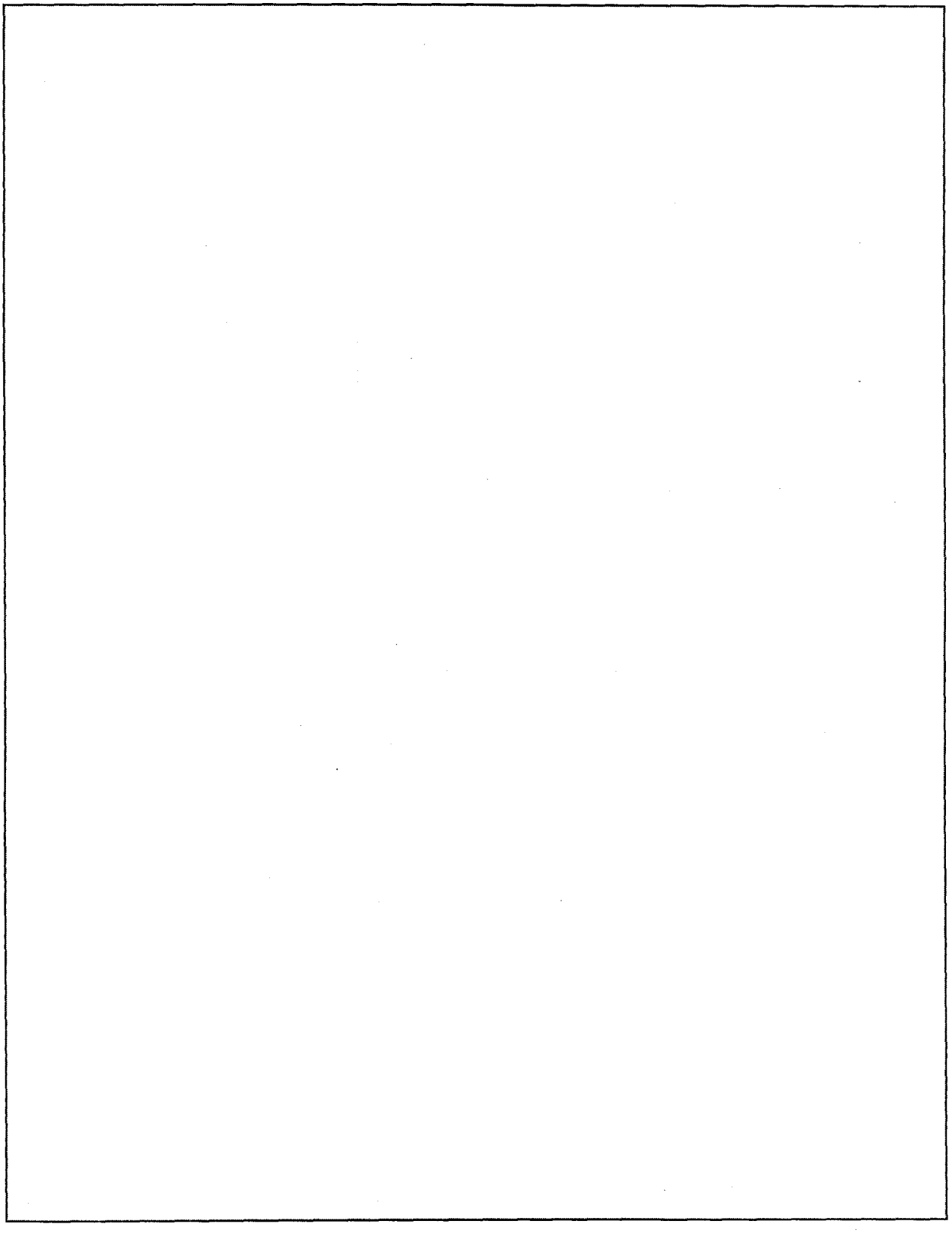

Comparison of the Measured and Analytical Response Profiles of a 3.3 to 15.5 μ Imaging System and the Effect of Detector Diffusion

C. F. Bruce Jr.
Jet Propulsion Laboratory, Pasadena, CA 91109

ABSTRACT

This paper provides an overview of the Tropospheric Emission Spectrometer (TES) and its mission, as a part of NASA's Earth Observing System (EOS). The design of the re-imaging system and its detectors and the test set-up used to characterize the field of view response will be presented. Measured system optical response profiles will be presented for each of the four infrared spectral bands (3.5-5.3, 5.1-9.1, 8.3-12.2 and 11.1 – 15.4 μ) supported by TES. Specific emphasis will be placed upon the comparison of these measured optical response functions with the results of an analytic model or the reponse. The model includes a simple yet accurate representation of the detector response function, which includes the photo-generated electron's diffusion length.

1.0 INTRODUCTION

THE TES MISSION and INSTRUMENT ARCHITECTURE

The Tropospheric Emission Spectrometer (TES) instrument is one of four instruments scheduled to fly aboard the Earth Observing System (EOS), AURA satellite. AURA is currently scheduled for launch in January of '04. The goals of the EOS program have been summarized in five "research questions" as reviewed in the TES Science Requirements.

1) What are the nature and extent of land–cover and land-use change and the consequences for sustained productivity?

2) How can we enable regionally useful forecasts of precipitation and temperature on seasonal to inter-annual time frames?

3) Can we learn to predict natural hazards and mitigate natural disasters?

4) What are the causes and impacts of long-term climate variability and can we distinguish natural from human induced-drivers?

5) How and why are concentrations and distributions of atmospheric ozone changing?

Although TES may contribute to answering all five questions, TES is specifically designed to address item five and it will do this by providing global maps of chemical concentration through out the troposphere every five days. In order to accomplish this feat, TES has been designed as a high resolution Fourier Transform Spectrometer (FTS) which is capable of collecting infrared spectra over a large region of the infrared spectrum from 3.3 to 15.4 microns at high spectral resolution (.025 cm^-1).

The primary objective is to measure the global three-dimensional distribution of concentration of a large number of molecules important to tropospheric physics and chemistry. These important molecular species include: ozone, nitric oxide, nitrogen dioxide, nitric acid, water vapor, carbon monoxide, methane and carbon dioxide for the determination of atmospheric temperature. TES will accomplish this through a series of nadir and limb measurements using 16 pixel, linear detector arrays in each of four infrared bands. In the limb view the 16 pixels' IFOV will rise from the earth's surface to ~30 km at the top of the troposphere. Each pixel IFOV will have a spatial extent of 2.3km high by 23 km parallel to the earth's surface at the limb. In the nadir view the pixel IFOV is 0.5 km by 5.0 km.

THE TES OPTICAL CONFIGURATION

The TES optical system is divided into four major sub-elements; the pointing mirror and fold, the input telescope, the interferometer, and the Focal Plane Opto-Mechanical Assemblies (FPOMA). A drawing of the TES optical system is provided in figure 1.0.

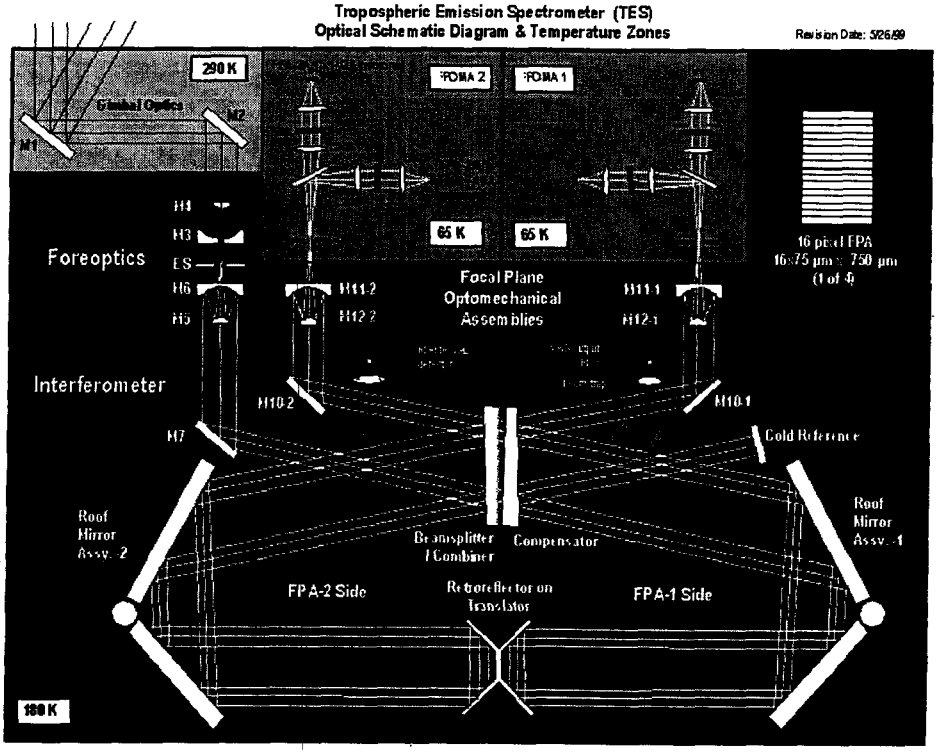

Figure 1.0 - TES Optical Layout and Temperature Zones

There are two FPOMAs, which collect the output signal from the interferometer, band limit the light and re-image the signal onto an array of detectors. A cross sectional view of the FPOMA with its temperature zones identified is provide in Figure # 2.0 along with a mechanical schematic of the exterior of the FPOMA. The output from the interferometer enters the FPOMA through an all aluminum F/8 Cassegrain telescope operating at 177K. The light

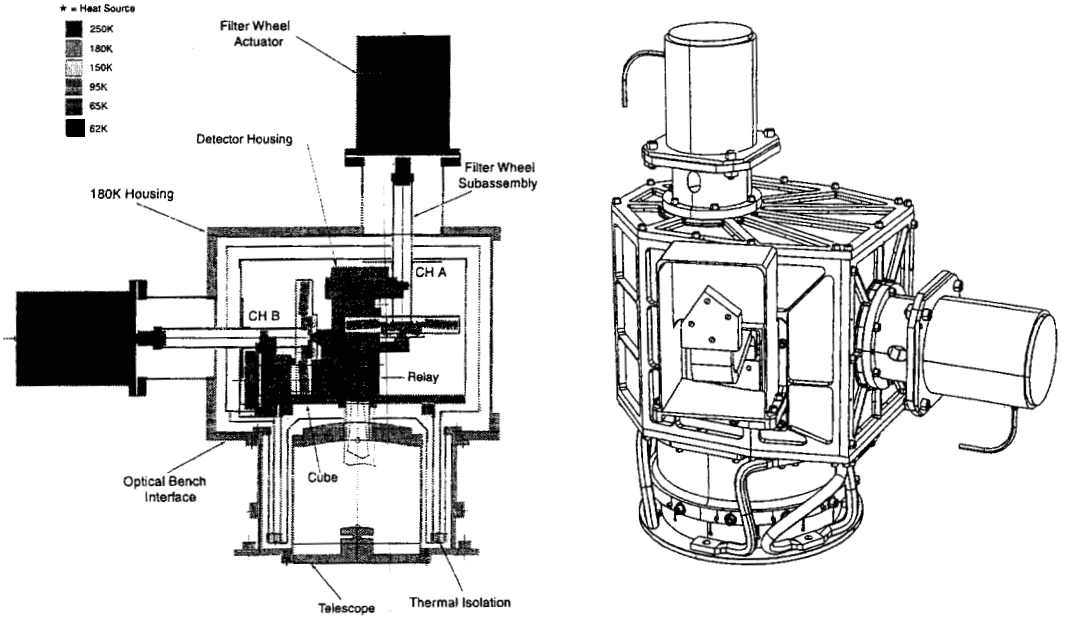

Figure 2.0 – FPOMA Cross Section and Exterior View

from the telescope is re-imaged at a 65K field stop after which a dichroic beam splitter divides the light. The beam then enters one of two F/2 relays, which re-collimates the light before sending it through any of a number of filters in the cold filter wheel assembly. The light is then re-imaged onto the detector array at F/2. The FPOMA pupil is re-imaged at the cube corner in the interferometer. Optical ghost were designed to be < 0.1% within the field by tilting filters (3.5 deg.) and adjusting the field lenses curvatures. The filters and dichroics are also wedged to prevent optical channeling. The 1A & 2 A band relay elements are ZnSe, the 1B relay elements are Germanium and the 2B relay elements are CdTe. The Space Dynamic Laboratory provided the FPOMAs to JPL under contract.

THE DETECTOR ARRAYS

The TES detector arrays are housed inside the FPOMAs at the focus of each relay. The detector arrays are implemented with a detector amplifier topology that includes one differential J-FET buffered transimpedance amplifier (TIA) per detector element.

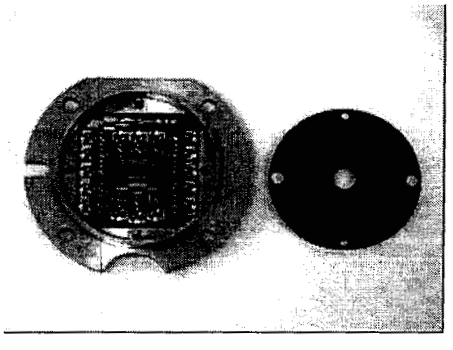

Picture 1.0 – The 1A Detector and Package

The J-FETS, the feedback resistor and decoupling capacitors are placed with the linear detector arrays onto a ceramic, multilayer board (CMLB). A Be flange is mated to the CMLB using an adhesive. The Be flange provides the mechanical and thermal interfaces for the detector package. This detector package is shown in Picture 1.0. A low thermal conductance, flex print cable, made of Constantan and Kapton, connects the detector package with the warm amplifier board. The detector parameters for each of the four spectral bands are summarized in Table 1.

Parameter	1A	2A	1B	2B
x	0.283	0.2274	0.2207	0.204
Temperature (K)	65	65	65	65
Detector Optical Area (μm^2)	75 x 750	75 x 750	75 x 750	75 x 750
Detector Band Pass (μm)	3.3 - 5.3	5.1 - 9.1	8.3 - 12.2	11.1 - 15.5
Peak D*($Hz^{.5}$ cm/W)	1.0 E13	3.9 E12	1.6 E12	3.9 E11
QE (%)	70	65	65	60
Diffusion length (μm)	15	20	20-25	25-30
Absorber Thickness (μm)	8	10	12	14

Table 1.0 TES Detector Parameters

The detector arrays for TES are based on a HgCdTe, double-layer planar heterostructure (DLPH) with a lateral collection architecture.

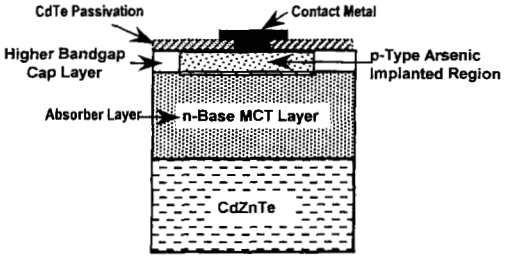

Figure 1. Schematic cross section of passivated p-on-n planar arsenic-doped HgCdTe Double Layer Planar Heterostructure (DLPH) diode.

Figure 3.0 – FPOMA Cross Section and Exterior View

The key feature of the DLPH approach is the planar p/n device geometry with a wide-bandgap surface layer covering the narrow-bandgap active layer. The layers are all grown n-type by MBE. The formation of planar p-on-n photodiodes is achieved by selective area arsenic (As) ion-implantation through the cap layer into the narrow gap base layer. A thin polycrystalline MBE deposited CdTe layer provides the device passivation. Holes are then etched in the CdTe layer, and ohmic contacts are deposited. The wafer is then over coated with ZnS, which serves to provide better adhesion for the interconnect metal. After etching via holes in the ZnS to expose the ohmic contact metal, the interconnect metal is deposited. The process is completed with a backside polish and deposition of a backside anti-reflection (AR) coating. The Rockwell Science Center of Rockwell International provided the detector assemblies to JPL under contract.

2.0 CRYOGENIC TEST SYSTEM

Once the flight detectors were integrated into the flight FPOMAs it was necessary to align the detectors to each of the boresight vectors of the FPOMAs and to each other within the FPOMAs. Data on the detector location and FPOMA bore sight were collected by a cryogenic test set which simulated the FPOMA interface with the TES instrument, thermally and mechanically. The test set also provides a target stimulus and controller. The stimulus consisted of an ambient three axis slit scan mechanism a blackbody and a data acquisition system. The test chamber is a 4' vacuum chamber with a ZnSe window. In side the scum chamber is a warm collimator with an EFL=100mm,

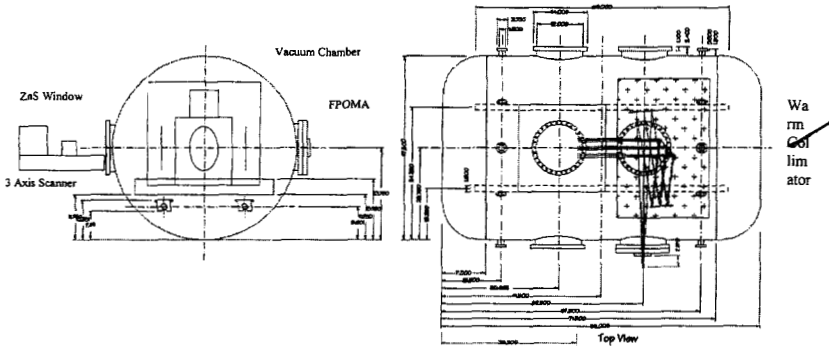

Figure 4.0 – FPOMA Cross Section and Exterior View

a 180K fold mirror on a commercial adapted to vacuum cryogenic operation and a 180K reference reflector polished into the Invar interface with the FPOMA.

The FPOMA and detectors require three thermal interfaces. The mounting interface at the entrance of the telescope is an invar interface at 177K. This interface was simulate with an invar plate cooled to 177K through a GN2, aluminum/copper transfer tube with a braded copper flex links so as to minimize the distortion of the Invar plate. This was critical since the interface to the FPOMA was specified to be flat to 0.1 thousands of an inch. The under side of this Invar plate was parallel to the top surface interface to less than 1 milliradian and polished to an optical quality surface approaching 1 wave peak to peak. This annular reference surface was used to established the boresight vector of the FPOMAs and provide a reference for the location of the center of each of the 16 pixel arrays.

A 230K Al thermal shield cooled by a GN2 transfer system surrounds the entire FPOMA. The detectors are cooled to their 65K operating temperature through a copper strap, which was isolated by G10 stand offs and driven by a helium transfer system. The temperature was monitored at the end of the copper strap, which interfaced to the Al cold link of the FPOMA. The temperature control as stable to < +/- 1 K through most of the testing.

The optical back ground to the FPOMA was limited to levels similar to those expected from the instrument configuration. This was accomplished through the use of a 180K-fold mirror and an F/10 tube sunk to the 180K-heat loop. The data was acquired through a mutli-channel digital voltmeter, which scanned through the 32 detectors out puts. A PC with custom software managed the acquisition of data and stepped the positioning stage, which held the slit. The software provided control through automated macros and a real time plotting capability.

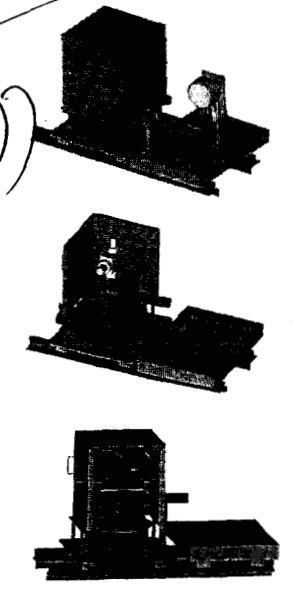

Figure 5.0 – Test Set

detailed drawing not ok

too detailed

whose information? the contractor's

3.0 TEST RESULTS

The final data set collected prior to delivery of the FPOMAs to the interferometer integration are presented. A blackbody at 325 K illuminated the slit. In FPOMA 1, figure 6.0, the 1A1 and 1B1 filters were selected coving the pass bands of 4.44 - 5.26 microns and 9.52 - 12.20 microns respectively.

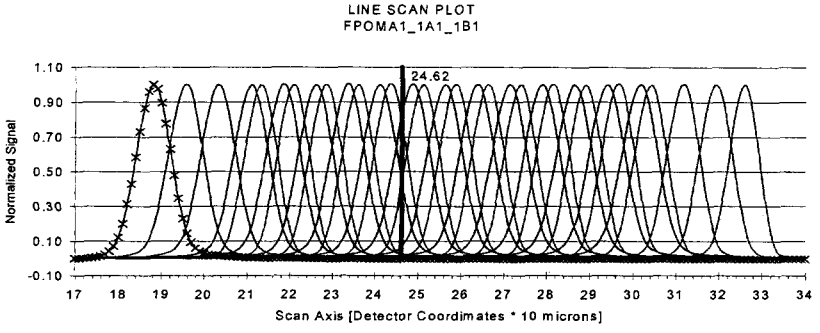

Figure 6.0 – FPOMA1, Spatial Response Functions

The data for these scans was acquired at each 10-micron step of the slit. These sample points are explicitly shown for the first response function in each plot. Each scan required approximately 20 min to acquire. One high resolution scan with 1.0 micron steps of the slit was acquired to verify that there was no high frequency spatial information in the pixel response functions. This data (not shown) supports the use of the interpolated lines as accurate representation of the data. The remainder of the data will be plotted as continuous functions for visual simplicity. The data for FPOMA1 shows a 225-micron misalignment in this axis. The response functions for each pixel with in

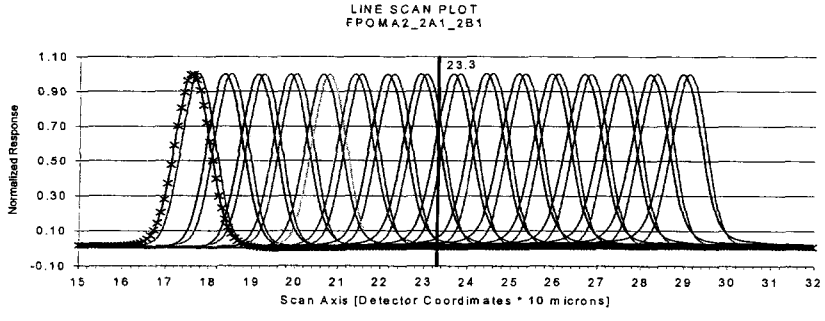

Figure 7.0 – FPOMA2, Spatial Response Functions

a particular optical band pass are very uniform. The data for FPOMA 2, Figure 7.0, reveals a residual misalignment of 2 and 6 microns for the 2B1 and 2A1 channel respectively. In this case the 2A1 and 2B1 filter were used giving optical pass bands of 7.55 – 9.10 microns and 11.11 – 15.38 microns respectively. Again the uniformity of detector response functions is excellent across the arrays.

4.0 ANALYTICAL MODEL

An analysis was undertaken to compare the shape of the measured response functions with the theoretically predicted response functions. The method chosen for the analysis is to convolve the measured slit function with the theoretical optical response function of the FPOMA and the detector response function. An illustration of these functions is provided in figure 8.0. The measured data and analytic functions are then compared in section 5.0.

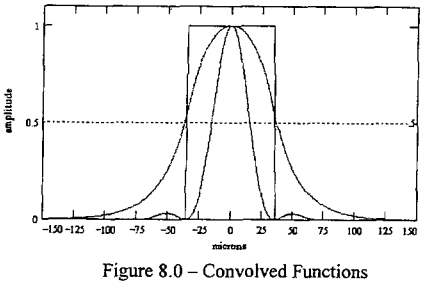

Figure 8.0 – Convolved Functions

The slit function is defined as a normalized boxcar function of width equal to the slit width. The slit width was measured to be 70 microns. This function is the same for all convolutions. The detector response function is also normalized and is calculated by equation 1.0. This function is an excellent representation of a thin detector with a junction length greater than the photo-generated electron's diffusion length. The function can be viewed as the probability density for the collection of a photoelectron by a detector junction of length J_d. The

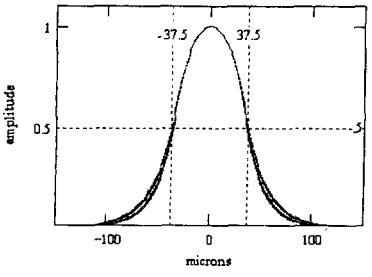

Figure 9.0 – Detector Response Functions

$$D(x,X,L_d) := \left| \int_{\frac{-J_d}{2}}^{\frac{J_d}{2}} \exp\left[-\frac{|(x-X)-s|}{L_d} \right] ds \right| \quad (1.0)$$

probability of any one collection is ~exp $(-x/L_d)$ integrated over the junction length (J_d). L_d is the diffusion length of the photo-generated electron and x is the vector from the electron's position to the detector junction. Figure 9.0 shows detector response functions with L_d = 17,18,20 and 21 microns. The optical response function for the FPOMA is calculated as diffraction limited with a centrally obscured, circular aperture at F#2 (equation 2.0). This response function is then integrated over the entire optical pass band and weighted by the black body function (equation 3.0) and normalized to unity (equation 4.0). The resulting normalized; chromatic optical response functions are shown in figure 10.0.

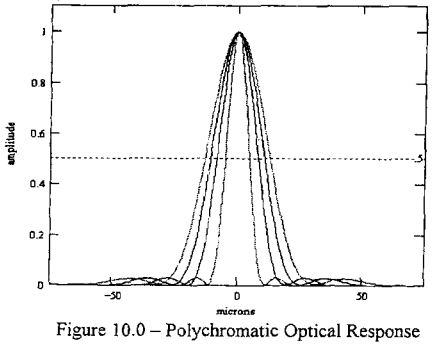

Figure 10.0 – Polychromatic Optical Response

$$S(x,y,X,\lambda) := \left| \left[\frac{1}{(1-\varepsilon^2)^2} \right] \left[\frac{2 \cdot J1\left[\frac{\pi \sqrt{(x-X)^2+y^2}}{\lambda \cdot F} \right]}{\frac{\pi \sqrt{(x-X)^2+y^2}}{\lambda \cdot F}} - \varepsilon^2 \left[\frac{2 \cdot J1\left[\left[\frac{\pi \sqrt{(x-X)^2+y^2}}{\lambda \cdot F} \right] \cdot \varepsilon \right]}{\left[\frac{\pi \sqrt{(x-X)^2+y^2}}{\lambda \cdot F} \right] \cdot \varepsilon} \right] \right]^2 \right| \quad (2.0)$$

$$SS(x,y,X,\lambda_1,\lambda_2) := \frac{\int_{\lambda_1}^{\lambda_2} B(\lambda,T) \cdot S(x,y,X,\lambda)\, d\lambda}{\int_{\lambda_1}^{\lambda_2} B(\lambda,T) \cdot 1\, d\lambda} \quad (3.0)$$

5.0 COMPARISON of RESULTS

The above functions were convolved for each of the four optical bands. Figure 11.0 shows a direct comparison between the analytic and measured response functions for each band. A diffusion length of 17 was assumed for all

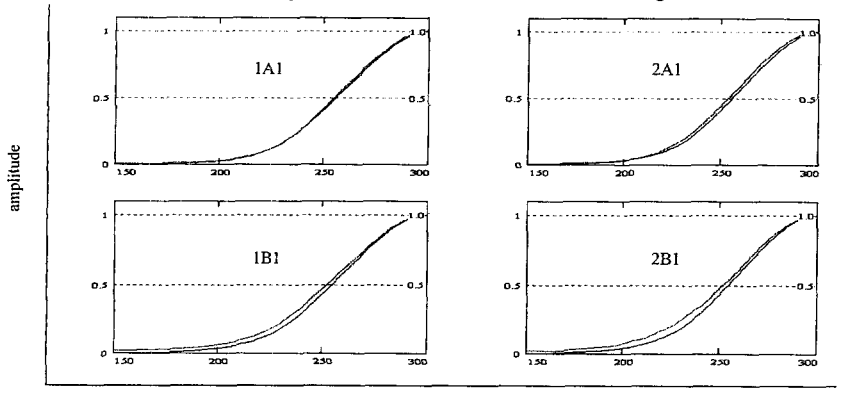

the bands. Only the left half of the optical response function is shown in order to improve the visible detail in the plots. The band 1A results are nearly identical to the theoretical predictions for a diffraction limited system and a 17-micron detector diffusion length. In each of the other cases the theoretical response function is larger than the measured data by an amount, which increases with wavelength from 1A to 2A to 1B and finally to 2B. The 2B

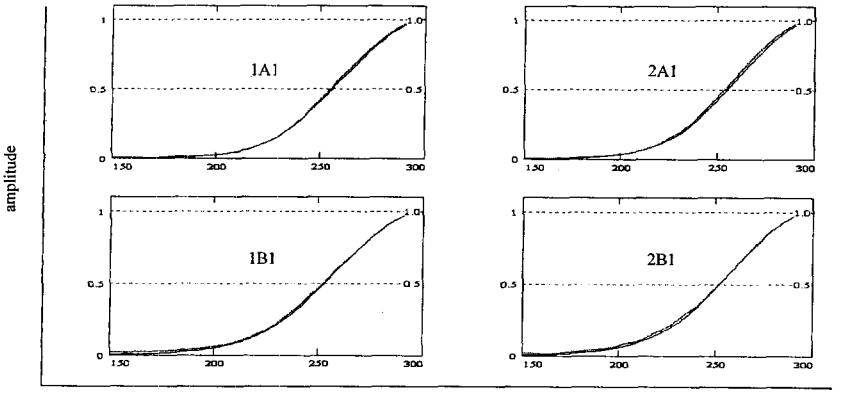

exhibits the largest variance with the analytic result. Since the polychromatic response function has already accounted for the wavelength dependence of the analytic optical response function we postulate that the detector diffusion length is responsible for the observed discrepancy. The detector diffusion length parameter is then selected to provide the best fit to the measured response data for each band. The diffusion length, which provides the best fits are for the 1A, 2A, 1B and 2B, bands respectively are 17, 18, 20 and 21 microns. The results are shown in figure 12.0.

6.0 IMPLICATION for DETECTOR DIFFUSION

As shown in table 2.0 the actual diffusion length for each of the detectors is considerably larger than the diffusion lengths selected to fit the spatial response data shown in figure 12.0

Detector	Detector L_d (μm)	Fitting L_d (μm)	Absorber Depth (μm)
1A	15	17	8
2A	20	18	10
1B	20-25	20	12
2B	25-30	21	14

Table 2.0 Detector Parameters

Clearly the actual variability in the detector diffusion length, as shown in figure 13.0, would have a significant impact on the system response functions. However, the data shows that it does not and indeed the measured and predicted response functions are very similar without any lateral diffusion length fitting. In fact, if the detector response model was a two-dimensional model the absorber depth, which also increases with wavelength, might be the actual factor accounting for the slight increase in detector response function with wavelength.

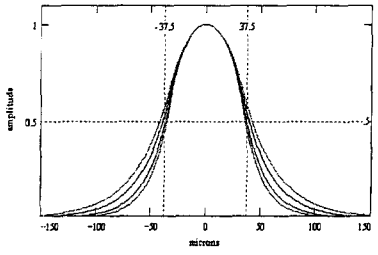

Figure 13.0 – Detector Response Functions

7.0 SUMMARY

ACKNOWLEDGEMENT

The work described in this article was performed both at the Jet Propulsion Laboratory, California Institute of Technology and at its subcontractors under contract with the National Aeronautics and Space Administration.

Reference herein to any specific commercial product, process, or service by trade name, trade mark, manufacturer, or otherwise, does not constitute or imply its endorsement by the United States Government or the Jet Propulsion Laboratory, California Institute of Technology.

This work was funded by JPL Contract No.

REFERENCES

1. Holloway (H. Holloway, *J. Appl. Phys.*, **49**, 4264, (1978)
2. Reinhard Beer, TES, Scientific Objectives & Approach, Goals & Requirements Rev. 6, (1999)
3. J. Bajaj, etal, IRIS Specialty Group Infrared Detectors, ERIM, (1999).
4. W.V. McLevige, etal, 1999 IRIS Specialty Group Infrared Detectors, ERIM, (1999).
5. R. J. Briggs, Three-Dimensional Numerical Analysis of Diffusion Current and Quantum Efficiency of Small Area
6. $Hg_{1-x}Cd_xTe$ Photodiodes, IEEE, (1981)
7. Jet Propulsion Laboratory, National Aeronautics and Space Administration, Contract 960577, (1996)
8. S.P. Tobin, *IEEE Transaction*, ED-27, p. 43, (1980)
9. Internal Communication, Jet Propulsion Laboratory, David Rider, (1999)

Date: Thu, 17 Jul 2003 16:44:25 -0700
From: Carl F Bruce-Jr <Carl.F.Bruce-Jr@jpl.nasa.gov>
Subject: Updated Draft.
X-Sender: cbrucejr@mail2.jpl.nasa.gov
To: Linda.J.Worrel@jpl.nasa.gov
X-Mailer: QUALCOMM Windows Eudora Version 5.2.0.9
Original-recipient: rfc822;Linda.J.Worrel@jpl.nasa.gov

Linda,

Let me know if you think this is compliant.

Carl

Carl F. Bruce Jr.

MS 306-392
Jet Propulsion Laboratory - NASA
California Institute of Technology
4800 Oak Grove Dr.
Pasadena, CA 91109
---
(818) 354-5480 (voice)
(818) 393-4489 (fax)

 SPIE_Draft_2.doc

Comparison of the Measured and Analytical Response Profiles of a 3.3 to 15.5 μ Imaging System and the Effect of Detector Diffusion

C. F. Bruce Jr.
Jet Propulsion Laboratory, Pasadena, CA 91109
California Institute of Technology

ABSTRACT

This paper provides an overview of the Tropospheric Emission Spectrometer (TES) and its mission, as a part of NASA's Earth Observing System (EOS). The design of the re-imaging system and its detectors and the test set-up used to characterize the field of view response will be presented. Measured system optical response profiles will be presented for each of the four infrared spectral bands (3.5-5.3, 5.1-9.1, 8.3-12.2 and 11.1 – 15.4 μ) supported by TES. Specific emphasis will be placed upon the comparison of these measured optical response functions with the results of an analytic model of the response. The model includes a simple yet accurate representation of the detector response function, which includes the photo-generated electron's diffusion length.

Keywords: Detector, HgCdTe, Diffusion Length, Response

1. INTRODUCTION

1.1 THE TES MISSION and INSTRUMENT ARCHITECTURE

The Tropospheric Emission Spectrometer (TES) instrument is one of four instruments scheduled to fly aboard the Earth Observing System (EOS), AURA satellite. AURA is currently scheduled for launch in January of '04. The goals of the EOS program have been summarized in five "research questions" as reviewed in the TES Science Requirements[1].

1) What are the nature and extent of land–cover and land-use change and the consequences for sustained productivity?

2) How can we enable regionally useful forecasts of precipitation and temperature on seasonal to inter-annual time frames?

3) Can we learn to predict natural hazards and mitigate natural disasters?

4) What are the causes and impacts of long-term climate variability and can we distinguish natural from human induced-drivers?

5) How and why are concentrations and distributions of atmospheric ozone changing?

Although TES may contribute to answering all five questions, TES is specifically designed to address item five and it will do this by providing global maps of chemical concentration through out the troposphere every five days. In order to accomplish this feat, TES has been designed as a high resolution Fourier Transform Spectrometer (FTS) which is capable of collecting infrared spectra over a large region of the infrared spectrum from 3.3 to 15.5 microns at high spectral resolution (.025 cm^-1).

The primary objective is to measure the global three-dimensional distribution of concentration of a large number of molecules important to tropospheric physics and chemistry. These important molecular species include: ozone, nitric oxide, nitrogen dioxide, nitric acid, water vapor, carbon monoxide, methane and carbon dioxide which is used for the determination of atmospheric temperature. TES will accomplish this through a series of nadir and limb measurements using 16-pixel, linear detector arrays in each of four infrared optical bands. In the limb view the 16 pixels' IFOVs will rise from the earth's surface to ~30 km at the top of the troposphere. Each pixel's IFOV will have a spatial extent of 2.3km high by 23 km long, parallel to the earth's surface at the limb. In the nadir view the pixel IFOV is 0.5 km by 5.0 km.

1.2 THE TES OPTICAL CONFIGURATION

The TES optical system is divided into four major sub-elements; the gimbal optics, the fore optics telescope, the interferometer, and the Focal Plane Opto-Mechanical Assemblies (FPOMA). A drawing of the TES optical system is provided in figure 1.

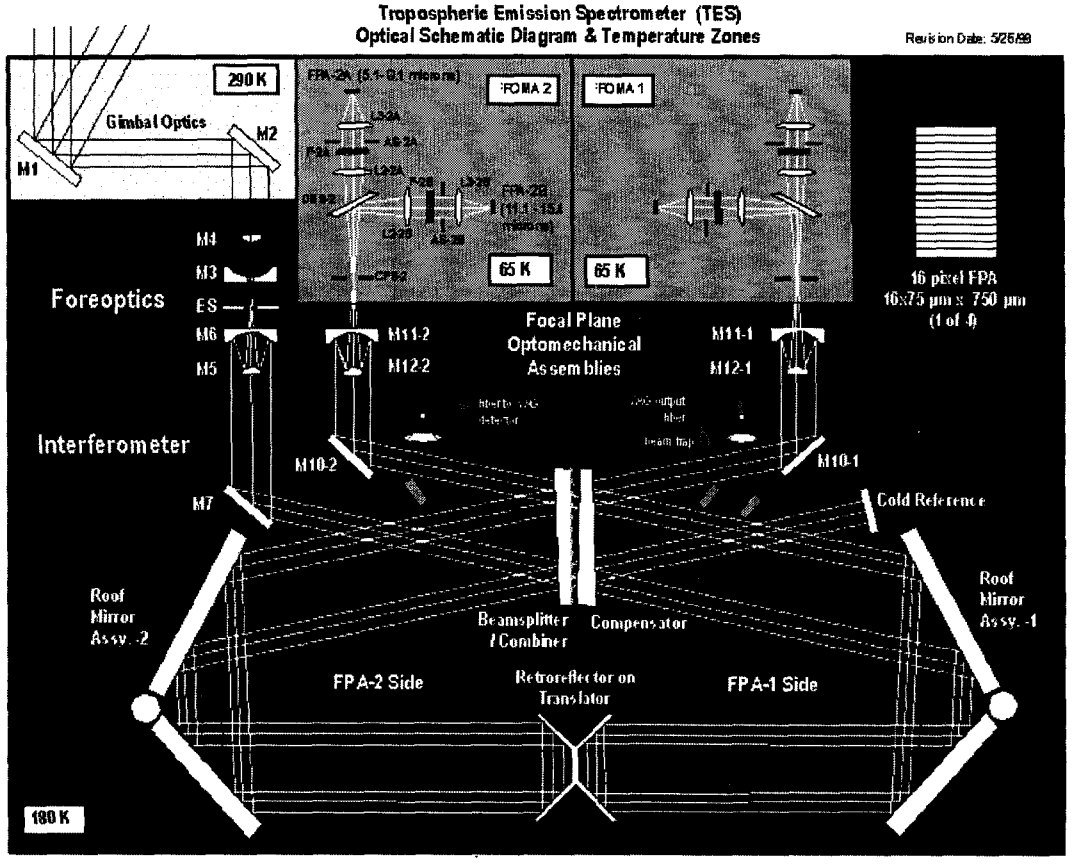

Figure 1: TES Optical Layout and Temperature Zones

There are two FPOMAs, which collect the output signal from the interferometer, band limit the light and re-image the signal onto an array of detectors. A cross sectional view of the FPOMA with its temperature zones identified is provide in figure 2 along with a mechanical schematic of the exterior of the FPOMA. The output from the interferometer enters the FPOMA through an all aluminum F/8 Cassegrain telescope operating at 177K. The light

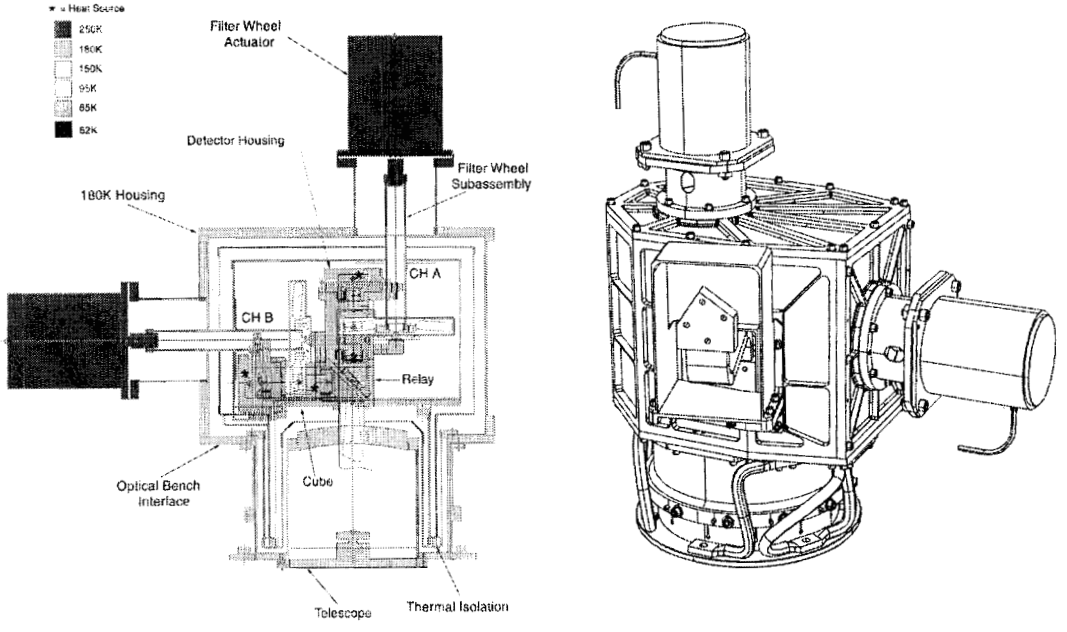

Figure 2: FPOMA Cross Section and Exterior View

from the telescope is re-imaged at a 65K field stop after which a dichroic beam splitter divides the light. The beam then enters one of two F/2 relays, which re-collimates the light before sending it through any of a number of filters in the cold filter wheel assembly. The light is then re-imaged onto the detector array at F/2. The FPOMA pupil is re-imaged at zero path difference in the interferometer. Optical ghost were designed to be < 0.1% within the field by tilting filters (3.5 deg.) and adjusting the field lenses curvatures. The filters and dichroics are also wedged to prevent optical channeling. The 1A & 2 A band relay elements are ZnSe, the 1B relay elements are Germanium and the 2B relay elements are CdTe. The Space Dynamic Laboratory provided the FPOMAs to JPL under contract.

1.3 THE DETECTOR ARRAYS

The TES detector arrays are housed inside the FPOMAs at the focus of each relay. The detector arrays are implemented with a detector amplifier topology that includes one differential J-FET buffered transimpedance amplifier (TIA) per detector element.

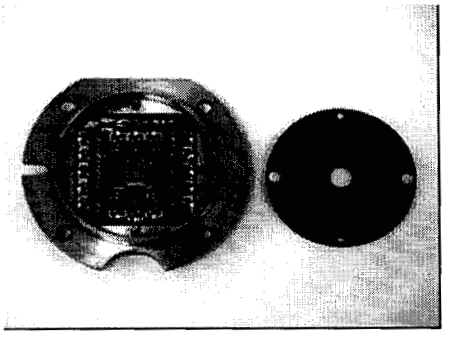

Picture 1: The 1A Detector and Package

The J-FETS, the feedback resistor and decoupling capacitors are placed with the linear detector arrays onto a ceramic, multilayer board (CMLB). A Be flange is mated to the CMLB using an adhesive. The Be flange provides the mechanical and thermal interfaces for the detector package. This detector package is shown in picture 1. The detector parameters for each of the four spectral bands are summarized in table 1.

Parameter	Detector - 1A1	Detector - 2A1	Detector - 1B1	Detector - 2B1
x	0.283	0.2274	0.2207	0.204
Temperature (K)	65	65	65	65
Detector Optical Area (μm^2)	75 x 750	75 x 750	75 x 750	75 x 750
Detector Band Pass (μm)	3.3 - 5.3	5.1 - 9.1	8.3 - 12.2	11.1 - 15.5
Diffusion length (μm)	15	20	20-25	25-30
Absorber Thickness (μm)	8	10	12	14

Table 1: TES Detector Parameters

The detector arrays for TES are based on a HgCdTe, double-layer planar heterostructure (DLPH) with a lateral collection architecture[2, 3, 4, 5].

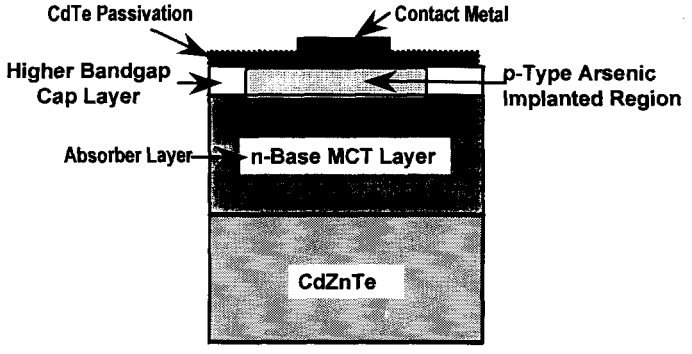

Figure 3. Schematic cross section of a P-on-N, HgCdTe (DLPH) diode.

The key feature of the DLPH approach is the planar p/n device geometry with a wide-bandgap surface layer covering the narrow-bandgap active layer. The layers are all grown n-type by MBE. The formation of planar p-on-n photodiodes is achieved by selective area arsenic (As) ion-implantation through the cap layer into the narrow gap base layer. A thin polycrystalline MBE deposited CdTe layer provides the device passivation. Holes are then etched in the CdTe layer, and ohmic contacts are deposited. The wafer is then over coated with ZnS. After etching via holes in the ZnS to expose the ohmic contact metal, the interconnect metal is deposited. The process is completed with a polish and deposition of a backside anti-reflection (AR) coating. A cross section of the detector is shown in figure 3. The Rockwell Science Center of Rockwell International provided the detector assemblies to JPL under contract[6, 7].

2. CRYOGENIC TEST SYSTEM

Once the detectors were integrated into the FPOMAs it was necessary to align the detectors to each of the boresight vectors of the FPOMAs and to each other within the FPOMAs. Data on the detector location and

FPOMA bore sights were collected by a cryogenic test set, which simulated the FPOMA interfaces with the TES instrument, both thermally and mechanically. The test set also provides a target stimulus and controller.

The stimulus consisted of an ambient, three axis scan mechanism which positioned the slit, a blackbody to illuminate the slit, a collimator to relay the slit to the FPOMA, and a data acquisition system. The test chamber is a 4' vacuum chamber with a ZnSe window near the focus of the collimator. In side the vacuum chamber is the warm collimator with an effective focal length of 1.0 m, a 180K fold mirror, and a 180K reference reflector polished into the Invar interface with the FPOMA.

The FPOMA and detectors require three thermal interfaces. The instrument-mounting interface at the entrance of the telescope is an invar interface at 177K. This interface was simulated with an invar plate cooled to while minimizing the distortion of the Invar plate. This was critical since the under side of this Invar plate was parallel to the top surface and polished to an optical quality. This annular reference surface was used to established the boresight vector of the FPOMAs and provide a reference for the location of the center of each of the 16 pixel arrays.

A 230K Al thermal shield cooled by a GN2 transfer system surrounds the entire FPOMA. The detectors are cooled to their 65K operating temperature through a copper strap, which was isolated by G10 stand offs and driven by a helium transfer system. The temperature was monitored at the end of the copper strap, which interfaced to the Al cold link of the FPOMA. The temperature control was stable to < +/- 1 K through most of the testing.

The optical background to the FPOMA was limited to levels similar to those expected from the instrument configuration. This was accomplished through the use of a 180K-fold mirror and an F/10 tube sunk to the 180K, cooling loop. The data was acquired through a mutli-channel digital voltmeter, which scanned through the 32 detectors outputs. A PC with custom software managed the acquisition of data and stepped the positioning stage, which held the slit. The software provided control through automated macros and provided a real time plotting capability.

3. TEST RESULTS

A single axis data set collected after the focus adjustments of the FPOMA were completed is presented. A blackbody at 325 K illuminated the slit. In FPOMA 1, figure 4, the 1A1 and 1B1 filters were selected coving the pass bands of 4.44 - 5.26 microns and 9.52 - 12.20 microns respectively. Scans are acquired from left to right.

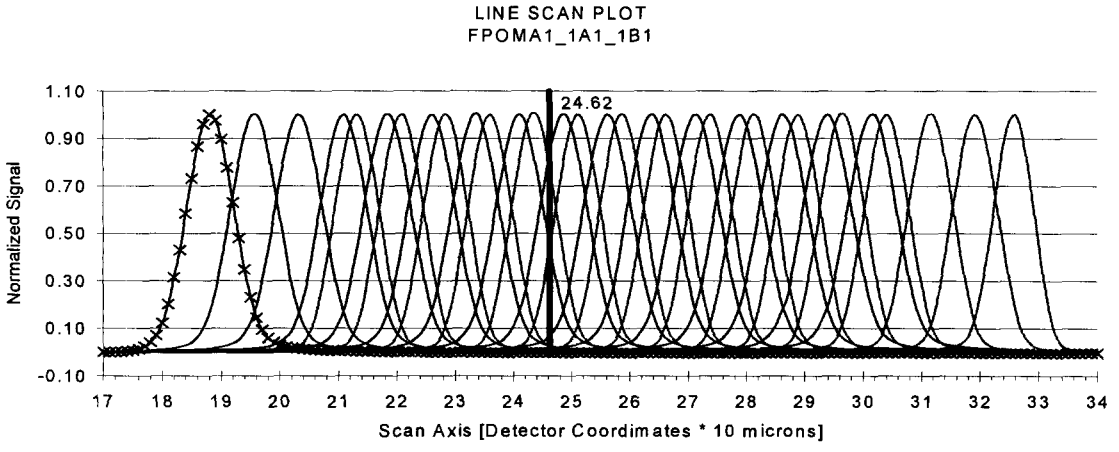

Figure 4: FPOMA1, Spatial Response Functions

The data for these scans was acquired at each 10-micron step of the slit. These sample points are explicitly shown for the first response function in each plot. Each scan required approximately 20 min to acquire. One high resolution scan taken with 1.0 micron steps of the slit was acquired to verify that there was no high frequency spatial information in the pixel response functions. This data (not shown) supports the use of the interpolated lines as an accurate representation of the data. The remainder of the data will be plotted as continuous functions for visual simplicity. The data for FPOMA1 shows a 225-micron misalignment in this axis. The response functions for each

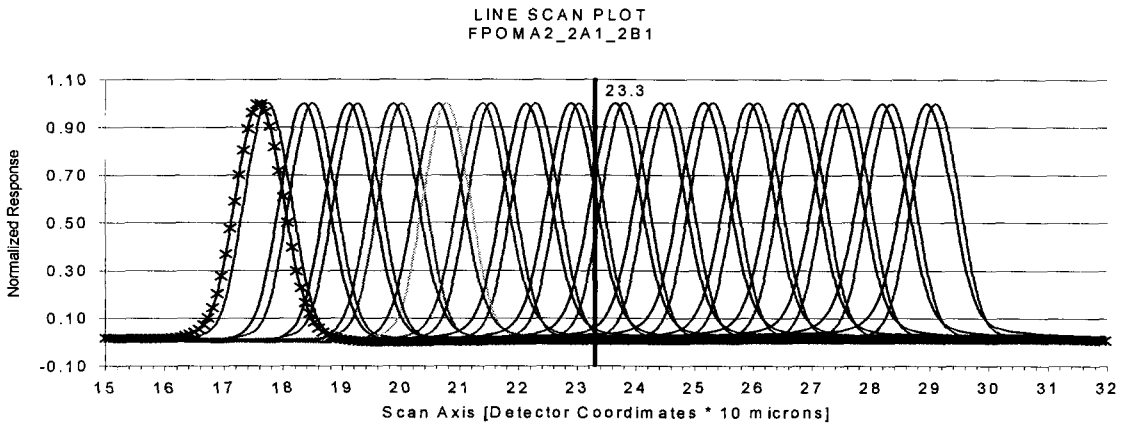

Figure 5: FPOMA2, Spatial Response Functions

pixel with in a particular optical band pass are very uniform in shape. All of the data was corrected for gain and offset on a per pixel basis. The data for FPOMA 2, Figure 5, reveals a residual misalignment of 2 and 6 microns for the 2B1 and 2A1 channel respectively. In this case the 2A1and 2B1filter were used. These filters define an optical pass band of 7.55 – 9.10 microns and 11.11 – 15.38 microns respectively. Again the uniformity of detector response functions is excellent across the arrays after a two-point, gain and offset correction.

4. ANALYTICAL MODEL

An analysis was undertaken to compare the shape of the measured response functions with the theoretically predicted response functions. The method chosen for the analysis is to convolve the measured slit function with the theoretical optical response function of the FPOMA and the detector response function. An illustration of these functions is provided in figure 6. The measured data and analytic functions are then compared in section 5.0.

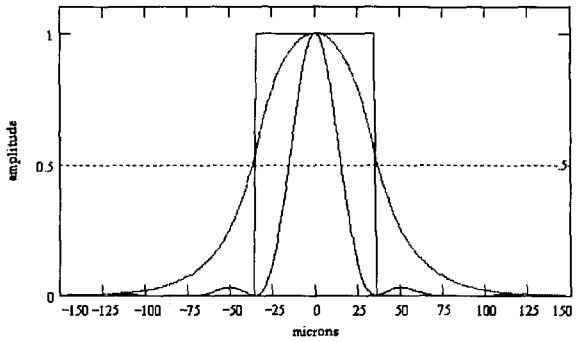

Figure 6: Convolved Functions

The slit function is defined as a normalized boxcar function of width equal to the slit width. The slit width was measured to be 70 microns. This function is the same for all convolutions. The detector response function is also normalized and is calculated by equation 1.0. This function is an excellent representation of a thin detector with a detector junction length greater than the photo-generated electron's diffusion length. The function can be viewed as the probability density for the collection of a photoelectron by a detector junction of length J_d. The probability of

any one collection is ~exp (-x/L_d) integrated over the junction length (J_d). L_d is the diffusion length of the photo-generated electron and x is the vector from the electron's position to the detector junction.

$$D(x,X,L_d) := \left| \int_{\frac{-J_d}{2}}^{\frac{J_d}{2}} \exp\left[-\frac{|(x-X)-s|}{L_d} \right] ds \right| \tag{1.0}$$

The optical response function for the FPOMA is calculated as diffraction limited with a centrally obscured, circular aperture at F/2 (equation 2.0)[8]. This response function is then integrated over the specific optical pass band and weighted by the black body function and normalized to unity (equation 3.0).

$$S(x,y,X,\lambda) := \left| \left[\frac{1}{\left(1-\varepsilon^2\right)^2} \right] \cdot \left[\frac{2 \cdot J1\left[\frac{\pi \cdot \sqrt{(x-X)^2+y^2}}{\lambda \cdot F} \right]}{\frac{\pi \cdot \sqrt{(x-X)^2+y^2}}{\lambda \cdot F}} - \varepsilon^2 \cdot \left[\frac{2 \cdot J1\left[\left[\frac{\pi \cdot \sqrt{(x-X)^2+y^2}}{\lambda \cdot F} \right] \cdot \varepsilon \right]}{\left[\frac{\pi \cdot \sqrt{(x-X)^2+y^2}}{\lambda \cdot F} \right] \cdot \varepsilon} \right] \right]^2 \right| \tag{2.0}$$

$$SS(x,y,X,\lambda_1,\lambda_2) := \frac{\int_{\lambda_1}^{\lambda_2} B(\lambda,T) \cdot S(x,y,X,\lambda)\, d\lambda}{\int_{\lambda_1}^{\lambda_2} B(\lambda,T) \cdot 1\, d\lambda} \tag{3.0}$$

5. COMPARISON of RESULTS

The functions defined in section 4.0 were convolved for each of the four optical bands. Figure 7 shows a direct comparison between the analytic and measured response functions for each band. A diffusion length of 17 microns

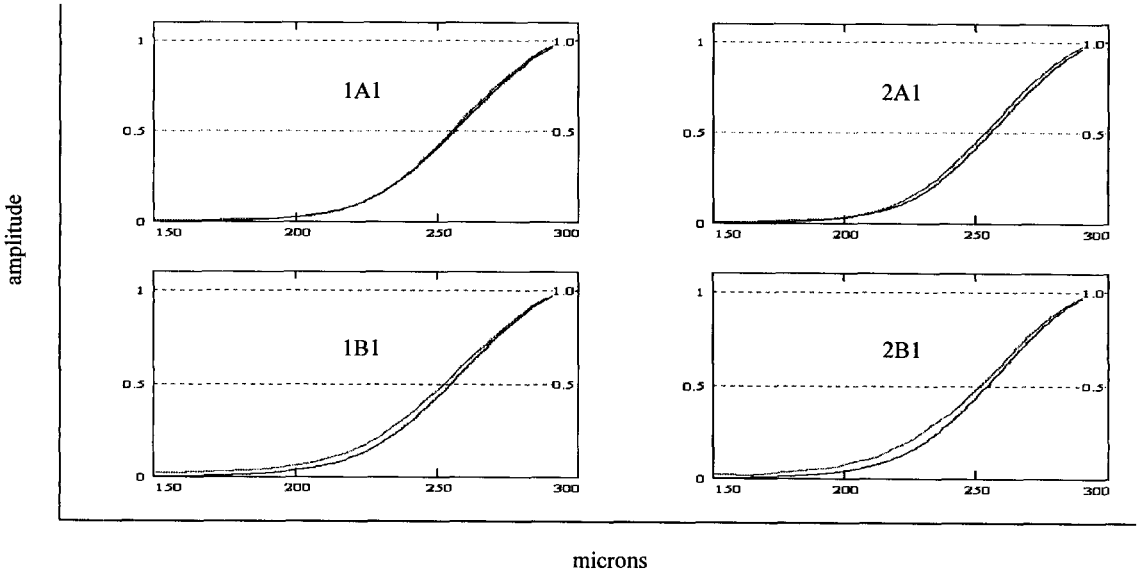

Figure 7: Comparison of measure and analytic response functions (Ld=17 microns)

was assumed for all the bands. Only the left half of the optical response function is shown in order to improve the visible detail in the plots. The band 1A results are nearly identical to the theoretical predictions for a diffraction limited system and a 17-micron photo-generated electron diffusion length. In each of the other cases the measured response function is slightly broader than the analytic function by an amount, which increases with wavelength from 1A to 2A to 1B and finally to 2B. The 2B exhibits the largest variance with the analytic result. Since the polychromatic response function has already accounted for the wavelength dependence of the analytic optical response function and the slit function has no wavelength dependence we postulate that the detector diffusion length is responsible for the observed discrepancy.

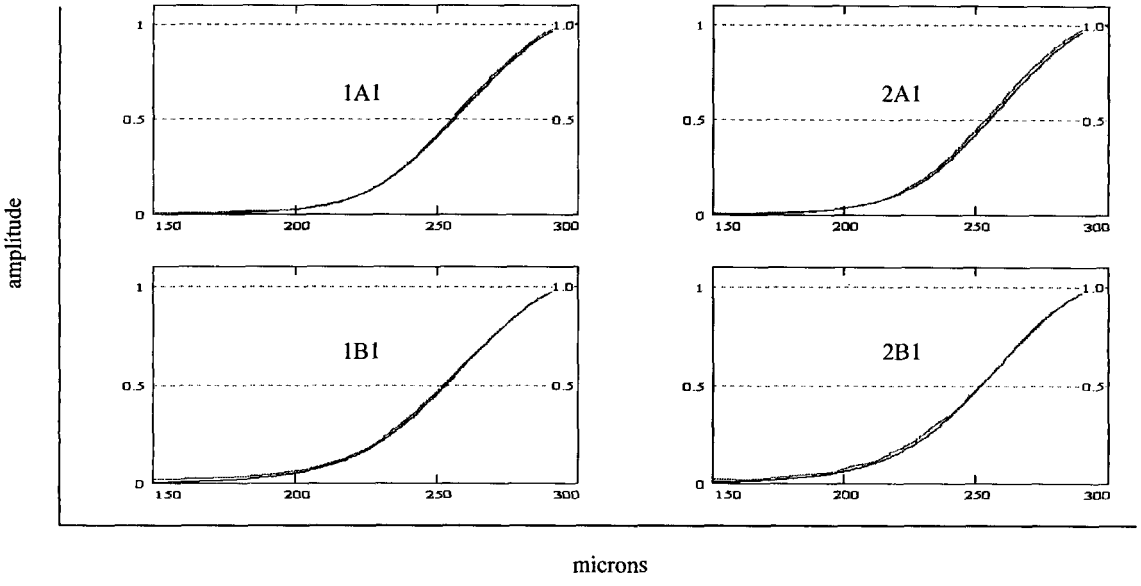

Figure 8: Comparison of measure and "best fit" analytic response functions (Ld=17,18,20,21 microns)

The detector diffusion length parameter is then selected to provide the best fit to the measured response data for each band. The diffusion length, which provides the best fits for the 1A, 2A, 1B and 2B, bands respectively are 17, 18, 20 and 21 microns. The results are shown in figure 8.

6. IMPLICATION for DETECTOR DIFFUSION

As shown in table 2.0 the actual minority carrier diffusion length for each of the detectors is considerably larger than the diffusion lengths selected to fit the spatial response data shown in figure 8.

Detector	Detector L_d (μm)	Fitting L_d (μm)	Absorber Depth (μm)
1A	15	17	8
2A	20	18	10
1B	20-25	20	12
2B	25-30	21	14

Table 2: Detector Parameters

Clearly, the actual variability in the detector diffusion length, as shown in figure 9, would have a significant impact on the system response functions. However, the data shows that it does not. In fact, the measured and predicted response functions are very similar without any lateral diffusion length fitting. If the detector response model was a two-dimensional model, the absorber depth, which also increases with wavelength, might be the actual factor accounting for the slight broadening of the detector response function with increasing wavelength. In additions the

detector minority carrier diffusion length may not be the same value as the photo-generated electron diffusion length[9] particularly away from the junction and so the use of the minority carrier diffusion length may result in an over estimate of the detector response function width. As well, for the TES architecture the effect of neighboring pixels tends to reduce the spatial extent of an individual detector's response function much in the same way a guard band may be used to reduce the spatial extend of a pixel. For example, if an electron appears half way between two detector junctions only one junction will collect that electron and thus neighboring pixels through a competition for the signal, limit one another's spatial response function.

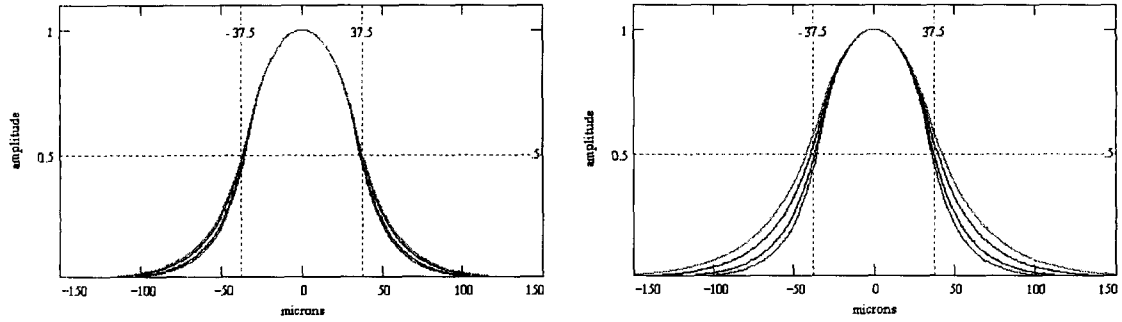

Figure 9: Detector Response Functions (Left: L_d=17,18,20,21μ) (Right: L_d = 17,20,25,30μ)

7. CONCLUSION

The field of view response of two cryogenic imaging systems covering four optical band passes were characterized. Each band pass has an HgCdTe detector array with a different cutoff wavelength. The complete field of view response was characterized and compared to an analytic model of the response function. It was determined that the variation of detector diffusion between optical bands did not significantly broaden the field of view response of this nearly diffraction limited system.

ACKNOWLEDGEMENT

The work described in this article was performed both at the Jet Propulsion Laboratory, California Institute of Technology and at its subcontractors under contract with the National Aeronautics and Space Administration.

Reference herein to any specific commercial product, process, or service by trade name, trade mark, manufacturer, or otherwise, does not constitute or imply its endorsement by the United States Government or the Jet Propulsion Laboratory, California Institute of Technology.

This work was funded by JPL Contract No. TBD

REFERENCES

1. Reinhard Beer, TES, Scientific Objectives & Approach, Goals & Requirements Rev. 6, (1999)

2. J. Bajaj, etal, IRIS Specialty Group Infrared Detectors, ERIM, (1999).

3. W.V. McLevige, etal, IRIS Specialty Group Infrared Detectors, ERIM, (1999).

4. C.F. Bruce, etal, Infrared Detector Assemblies for the Tropospheric Emission Spectrometer, IEEE Aerospace Conference, IEEE, (2000)

5. Holloway (H. Holloway, *J. Appl. Phys.*, **49**, 4264, (1978)

6. Jet Propulsion Laboratory, National Aeronautics and Space Administration, Contract 960577, (1996)

7. Jet Propulsion Laboratory, National Aeronautics and Space Administration, Contract TBD, (2002)

8. D.J. Schroeder, *Astronomical Optics*, Ch. 10, Academic press, Inc., San Diego, 1987

9. Marion,